

## Asymmetric transmission of electrons in ballistic graphene

Xin Tong,<sup>†</sup> Ling Zhou,<sup>†</sup> Ruihuang Zhao<sup>✉</sup>, Jiaxin Wang, Jinhu Luo, and Junjie Du<sup>✉\*</sup>

*State Key Laboratory of Precision Spectroscopy, School of Physics and Electronic Science,  
East China Normal University, 200062 Shanghai, China*



(Received 24 January 2024; revised 27 May 2024; accepted 13 August 2024; published 10 September 2024)

Semiconductor *p-n* junctions with depletion zones have gained widespread use as a conventional way to give rise to electron asymmetric transmission. However, the approach is not applicable to monolayer graphene due to its characteristic feature of zero band gap. Asymmetric transmission in ballistic graphene therefore remains elusive to date. Here a simple approach based on the engineering of a four-layer array of quantum dots is proposed. Despite the array having few layers, it has the combined functionality of electron metasurfaces and band-gap materials with the symmetry breaking of spatial inversion, the extraordinary properties enabling electron asymmetric transmission. Our results open up the possibility of realizing electronic units dependent on the one-way effect and show great application potential with nearly perfect efficiency and simple design.

DOI: 10.1103/PhysRevApplied.22.L031003

Graphene has been viewed as a promising platform for developing alternative electronic devices because of exceptionally high intrinsic mobility and electrical conductivity [1]. Electrons in ballistic graphene behave in close analogy to light because of their shared linear dispersion relation. This similarity has inspired the development of quantum electron optics by application of enlightening ideas in optics to graphene. Various optically inspired functional units, such as two-dimensional electron microscopes [2], quantum switches [3], Fabry-Perot cavities [4], electron waveguides [5–7], beam splitters [8], and the Vesolago lens [9–12], have been demonstrated. However, the lack of a feasible scheme to achieve asymmetric transmission remains a long-standing problem in ballistic graphene. Consequently, numerous electronic elements based on asymmetric transmission, including rectifiers, demodulators, voltage regulators, and logic gates, are unavailable although they play a pivotal role in electronic devices and microelectronics technology, severely restricting the use of ballistic graphene in various applications.

Electron asymmetric transmission is conventionally achieved by the use of semiconductor *p-n* junctions. As a Dirac material, monolayer graphene is characterized by a zero band gap and cannot function as a semiconductor. Various band-gap-opening approaches have been explored theoretically [13–16] and experimentally [17] to convert graphene into a semiconductor. However, opening the band gap is challenged by how to maintain high charge-carrier mobility of graphene, although great

efforts have been made to achieve improved carrier mobility [18,19]. Another approach is to exploit the one-way characteristic of the topological states. This is feasible for bilayer graphene [20,21], but not for monolayer graphene, within which Dirac ballistic electrons can only exist. On the other hand, extensive research has been conducted to break Lorentz reciprocity of classical waves and realize asymmetric transmission. The available schemes for optical waves include the use of magneto-optical materials [22–25], spatiotemporal modulation of nonmagnetic structures [26–32], and Kerr or Kerr-like nonlinearity [33,34]. Spatiotemporal modulation [35] and lossy acoustic metasurfaces [36] have been applied to asymmetric transmission of acoustic waves. The approaches are fundamentally different from semi-conductor *p-n* junctions and topological properties. Inspired by the remarkable achievements in optics and acoustics, we explore an approach to achieve asymmetric transmission by breaking Lorentz reciprocity of ballistic electrons in monolayer graphene, without the need for full band gaps or topological states. However, the schemes developed in optics and acoustics cannot be directly applied to ballistic electrons that are subject to Klein tunneling [37]. Normally incident ballistic electrons can pass through any barrier with nearly 100% efficiency, almost independently of the barrier height due to Klein tunneling. Since Klein tunneling is inevitable, we might as well exploit the tunneling effect to allow the backward-propagating incident electrons to penetrate through the structure. The forward-propagating electrons are altered from normal incidence to oblique incidence by an electron metasurface positioned in front of a partial-band-gap material. The forward-propagating electrons are ultimately reflected by the band-gap material since Klein tunneling does not work at the oblique incident angle. Physically,

\*Contact author: phyjunjie@gmail.com

<sup>†</sup>These authors contributed equally to this work.

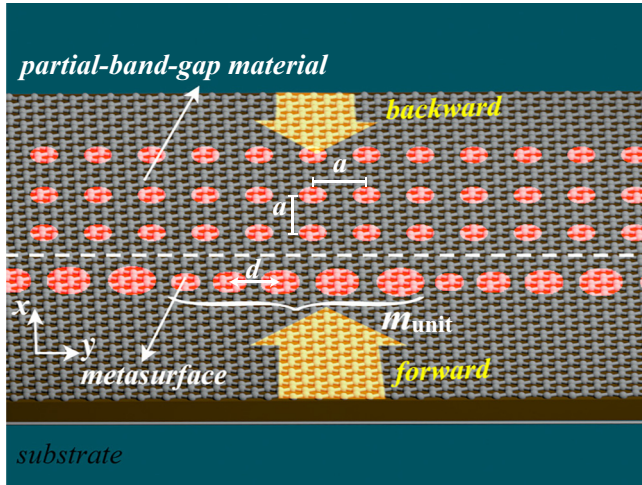


FIG. 1. Artificial engineered material composed of a four-layer array of QDs to achieve asymmetric transmission. QDs are denoted by the red circular regions. The front layer functions as a metasurface, whose unit cell consists of  $m_{\text{unit}}$  QDs with linearly increasing radius. The separation between adjacent QDs is  $d$ . The last three layers are a square-lattice array and provide a partial band gap. The same bias voltage is applied on all the QDs.

the whole structure has broken spatial-inversion symmetry with the metasurface appearing only in front of the band-gap material, leading to different transport properties of incident electrons in the forward and backward directions.

In this Letter, we use gate-defined quantum dots (QDs) with the same radius to constitute an artificial engineered material that has zero band gap like the host medium graphene and is responsible for offering a partial band gap. At the same time, QDs with gradually varying radius are arranged as unit cells that repeat periodically in a line to further form an electron metasurface, another kind of artificial engineered material. Electron metasurfaces can also be designed with the use of quantum dots that have the same radius but gradient-increasing bias voltages within a modulation period [38]. The electron metasurface and the band-gap material constitute a composite-structure system. Figure 1 schematically shows the composite structure, which has been divided functionally into a metasurface and a band-gap material by a dashed white line. The modulation period of metasurfaces is the length of their unit cell  $\Gamma = m_{\text{unit}}d$ , with  $d$  the spacing between adjacent QDs and  $m_{\text{unit}}$  the number of QDs in a unit cell. The band-gap material is a square-lattice array of QDs with lattice spacing  $a$ . To design the composite structure with asymmetric transmission properties for the incident electrons in the forward and backward directions, we investigate the electron behaviors in the band-gap material and the metasurface.

QDs have been widely used as meta-atoms and meta-molecules to gain a higher degree of manipulation freedom in graphene electronics [39–41]. The QDs used here are supposed to be smooth on the scale of the graphene's

intrinsic lattice constant, but sharp on the scale of the de Broglie wavelength. The low-energy electron dynamics can thus be described by the single-valley Dirac-Hamiltonian [42]

$$H = -i\hbar v_F \nabla \sigma + V_s \Theta(R_s - r), \quad (1)$$

with QDs with radius  $R_s$  expressed as the Heaviside step function  $\Theta(R_s - r)$ ,  $V_s$  the bias applied on them, and  $\sigma = (\sigma_x, \sigma_y)$  Pauli matrices. The electron scattering by an individual QD can be analytically calculated on the basis of Mie scattering theory [42]. Moreover, it has also been proved that the electron-scattering behavior of QDs remains nearly the same [43] when the transition distance is less than  $0.5R_s$ . In what follows, reduced units are used with  $\hbar = 1$  and Fermi velocity  $v_F = 1$ , and all the calculations involving multiple QDs are done with the rigorous multiple-scattering theory [42].

We first calculate the energy band structure of the band-gap material with  $R_s = 1$ , lattice constant  $a = 5$ , and bias  $V_s = 3$  in Fig. 2. An alternative representation  $\tilde{E} = Ea/2\pi v_F$  ( $v_F = 1$ ) is used for the electron energy  $E$ . The “light lines” in the  $\Gamma$ - $X$  and  $\Gamma$ - $M$  directions, displayed as solid red lines, are also given in Fig. 2, which illustrate the behaviors of low-energy ballistic electrons in primitive graphene. We see that the “light lines” intersect with the energy band at  $\tilde{E} = 0.33$  and  $\tilde{E} = 0.35$ . The intersection points represent electron momentum matching between primitive graphene and the band-gap material, and hence the incident electrons can penetrate through the material. The two intersection points divide the energy band structure into three energy ranges indicated by different background colors in Fig. 2. The oblique incident electrons, whose energy falls into different energy ranges, will be manipulated by the band-gap material in a different way. This can be understood by our investigating their equienergy-contour diagrams in the first Brillouin zone. Figure 3(a) gives the equienergy-contour diagram of the band-gap material in the energy range above the upper intersection—namely,  $\tilde{E}$  ranging from 0.35 to 0.5. The “light line” in the energy-band structure manifests itself as a series of concentric circles with radius proportional to energy  $\tilde{E}$ , which are the equienergy contours for electrons in primitive graphene. Two such equienergy circles are given for energy  $\tilde{E}_L = 0.35$  and  $\tilde{E}_L = 0.48$  in Fig. 3(a). One can see that the equienergy contours for the band-gap material and primitive graphene intersect at  $\tilde{E} = 0.35$ , in accord with the results in Fig. 2. On the other hand, for  $\tilde{E}$  larger than 0.35, the equienergy contour for primitive graphene does not intersect with that for the band-gap material in any direction. This is clearly shown by the equienergy circle at  $\tilde{E}_L = 0.48$ . This implies that there is a mismatch in electron momentum between the background and the band-gap material. Thereby, apart from the normal-incidence case, in which electrons will

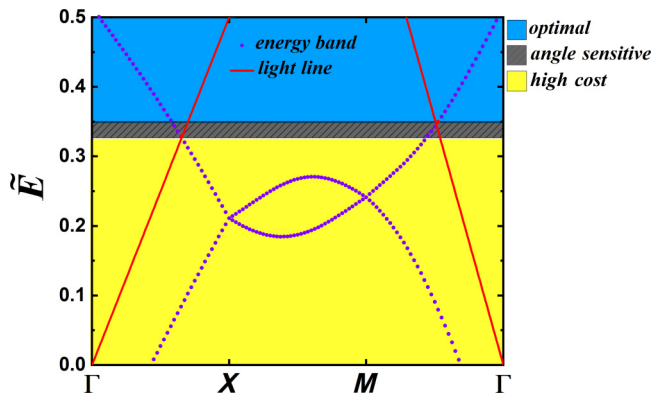


FIG. 2. Energy-band structures of the square array of QDs with QD radius  $R_s = 1.0$ . The lattice constant  $a$  is 5.0 and the bias voltage  $V_s$  applied on the QDs is 3.0. The “light lines” in the  $\Gamma$ - $X$  and  $\Gamma$ - $M$  directions are displayed as solid red lines, which show the energy-band structure of electrons in primitive graphene.

penetrate through the band-gap material because of Klein tunneling, oblique incident electrons will always be totally reflected. In the energy range between the upper and lower intersection points, the equienergy contours for the band-gap material and primitive graphene intersect more than once at a specific energy, as shown in Fig. 3(b). The intersections mean the incident electrons in this energy range are allowed to pass through the material not only under normal incidence but also at the corresponding oblique-incidence angles. Finally, we examine the energy range below the lower intersection point and present the equienergy-contour diagram for energies below 0.16 in Fig. 3(c). As a typical example, the equienergy circle at energy  $E_L = 0.1$  for primitive graphene is plotted. Similarly to the case in Fig. 3(a), no intersection occurs in any direction again.

On the basis of the above analysis, the intermediate energy range can be named the “angle-sensitive range” since the momentum can be matched at some oblique incident angles, thereby allowing the incident electrons to pass through the band-gap material at these incident angles. This is different from the upper and lower energy ranges, in which the momentum is not matched at an arbitrary angle of oblique incidence. However, the total reflection of electron waves results in different requirements for the band-gap material in the two energy ranges. In the lower energy range, Dirac electrons have wavelength several times or even tens of times the lattice constant, and thus the band-gap material must be thick enough to reflect the incident electrons totally. A great layer number of QDs is required, making the fabrication process costly. We therefore name it the “high-cost energy range”. Electrons in the upper energy range have wavelength comparable to the lattice constant, and a few-layer array of QDs can totally reflect the oblique incident electrons. From the results taken together, we find this is the optimal energy range for practical applications. In the subsequent simulations, the energy  $\tilde{E} = 0.48$  in the

optimal range is chosen. To illustrate the amazing ability in the optimal energy range, Figs. 4(a) and 4(b) illustrate the total transmission of a normally incident beam and the total reflection of a  $30^\circ$  obliquely incident beam, respectively, when they interact with the band-gap material comprising solely of three layers of QDs. Highly collimated electron beams have been experimentally achieved in graphene by the use of collinear pairs of slits with absorptive sidewalls between the slits [44].

We hope to achieve asymmetric transmission by exploiting the properties of the band-gap material that can guide normal incident waves while blocking oblique incident waves. To this end, we need to introduce another structure on the front side of the band-gap material to change the forward-propagating electrons from normal incidence to oblique incidence. The forward-propagating electrons will thus be blocked by the band-gap material, while the backward-propagating electrons remain at normal incidence and can pass through. The introduced structure is expected to be easy to fabricate and of high efficiency. Electron metasurfaces [38], formally a QD array in a line, is an excellent candidate that has a compact design and nearly perfect efficiency. The behavior of electrons in metasurfaces follows the generalized Snell’s law of refraction [45]

$$n_r \sin \theta_t - n_i \sin \theta_i = \frac{1}{k_0} \frac{d\Phi}{dx}, \quad (2)$$

where  $k_0$  is the magnitude of the free-space wave vector,  $\theta_i$  and  $\theta_r$  are, respectively, the angle of incidence and the angle of refraction, and  $n_i$  and  $n_r$  are the respective “refractive indices” of media on the incident and refraction sides of the metasurface. An  $x$ -directed effective wave vector (i.e., an effective momentum) is introduced in the presence of the phase gradient  $d\Phi/dx$  that is presented by the unit cells constituting metasurfaces. The momentum introduced by metasurfaces is imparted to the refracted electrons and causes the transmitted and reflected electron beams to be deflected at an angle. The bending angle depends on the direction and magnitude of the phase gradient. In a previous study [38], the phase gradient was obtained by means of unit cells containing QDs of the same radius but different applied bias voltages. Here another type of metasurface is proposed and used, whose unit cells consist of QDs with the same applied bias voltage but a linearly increasing radius gradient. Radius-varying metasurfaces and voltage-varying metasurfaces have the same performance. For the purpose of more options, we use a radius-varying metasurface in the following. Figures 4(c) and 4(d) compare the transmission of the normal-incidence electrons by an ordinary single layer of QDs and by a metasurface. All the QDs for the former have the same radius and bias voltages, with  $R_s = 1$  and  $V_s = 3$ , whereas the latter includes a series of unit cells in which the number of

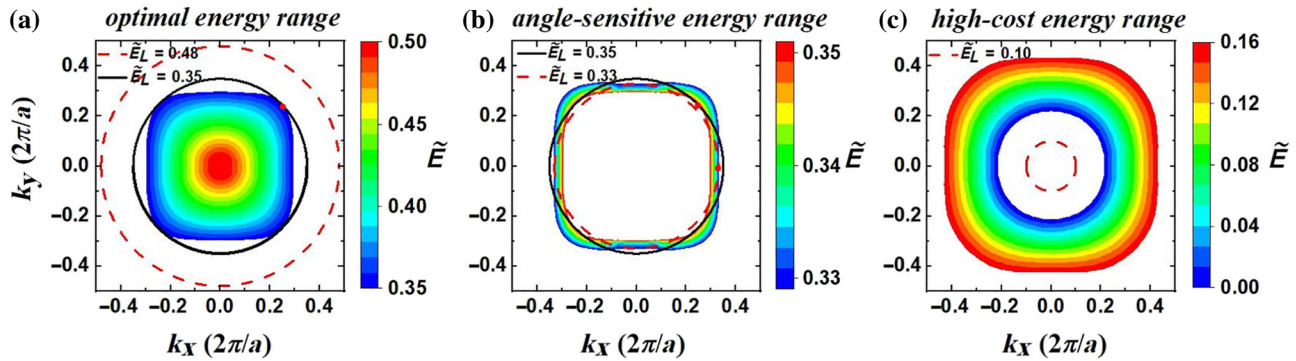


FIG. 3. Equienergy-contour diagrams of the same QD array as in Fig. 2 in the first Brillouin zone, corresponding to the energy ranges (a)  $0.35 < \tilde{E} < 0.50$ , (b)  $0.33 < \tilde{E} < 0.35$ , and (c)  $0 < \tilde{E} < 0.16$ . The equienergy contours for primitive graphene are given for  $\tilde{E}_L = 0.35$  and  $0.48$  in (a),  $\tilde{E}_L = 0.33$  and  $0.35$  in (b), and  $\tilde{E}_L = 0.10$  in (c). They are a representation of the “light lines” in the first Brillouin zone and manifest themselves as a circle.

QDs  $m_{\text{unit}}$  is 5 and their radius  $R_s$  linearly increases from 1 to 1.8 with bias voltage  $V_s = 3$  applied. The spacing  $d$  between the adjacent QDs is 4 in Figs. 4(c)–4(e) and the modulation period  $\Gamma$  in the metasurface is thus  $5d = 20$ . We see that the electron beam passes through the ordinary array without any change, but is bent by the metasurface. Although each unit cell contains only five QDs, it is shown that the metasurface has near-unit operating efficiency. This makes it possible to achieve perfect-efficiency asymmetric transmission with the simple structure. The bending angle can be precisely predicted for the designed metasurfaces. Figures 4(d) and 4(e) show the bending of the normal-incidence and oblique-incidence electron beams with the free-space wave number  $k_0$  ( $k_0 = E = 2\pi\tilde{E}/a$  in reduced units), respectively. For the normal-incidence case, a complete phase coverage from 0 to  $2\pi$  is obtained with an approximately constant phase difference  $\Delta\phi = 2\pi/5$  between neighbors [42]. Thus, the magnitude of the introduced wave vector in the  $x$  direction is given by  $k_x^{\text{add}} = d\Phi/dx = 2\pi/\Gamma = 0.1\pi$ , and the incident electron beam will be bent at an angle  $\theta_{\text{calc}} = \arcsin(k_x^{\text{add}}/k_0) = 31.4^\circ$ . For the oblique-incidence case with angle of incidence

$\theta_i = 30^\circ$ , the same unit cell creates a phase change of  $4\pi$ , and moreover, the phase increases gradually in the opposite direction, in contrast to the normal-incidence case in Fig. 4(d) [42]. Thus, the incident electron beam will be bent by the metasurface by  $\theta_{\text{calc}} = \arcsin(k_x^{\text{add}}/k_0) = -62.8^\circ$ , and consequently the transmitted electrons travel out at an angle of  $-32.8^\circ$ , as shown in Fig. 4(e). Here the positive and negative signs indicate the transmitted beams are located on different sides of the normal line. The travel directions of the transmitted beam in Figs. 4(d) and 4(e) agree well with  $\theta_{\text{calc}}$ .

We now integrate the band-gap material and the metasurface to construct a composite to realize asymmetric transmission. The separation between the metasurface and the band-gap material is the same as the lattice spacing of the band-gap material,  $a = 5$ . The metasurface is positioned in front of the band-gap material, and the forward-propagating electrons will first encounter the metasurface. After passing through the metasurface, the forward-propagating electrons are obliquely incident on the band-gap material and are totally reflected in Fig. 5(a) since the electron energy  $\tilde{E} = 0.48$  is in the optimal energy

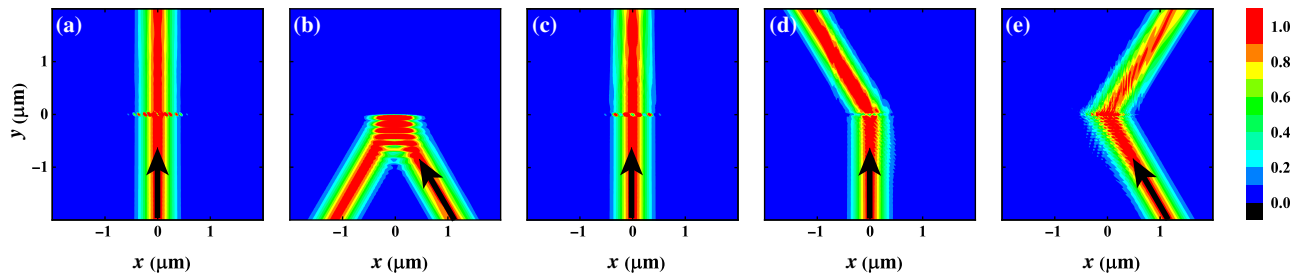


FIG. 4. Electron-density distribution around the band-gap material when it illuminated by a Gaussian beam at angle of incidence  $\theta_i$  (a)  $0^\circ$  and (b)  $30^\circ$ . The band-gap material consists of a three-layer array of QDs with QD radius  $R_s = 1$ , lattice spacing  $a = 5$ , and bias  $V_s = 3$ . Electron-density distribution around (c) an ordinary single layer of QDs and a metasurface when it is illuminated by a Gaussian beam at angle of incidence  $\theta_i$  (d)  $0^\circ$  and (e)  $30^\circ$  (e). The ordinary single layer is composed of QDs with the same radius  $R_s = 1$  and the same applied bias voltage  $V_s = 3$ . The metasurface consists of a series of unit cells in which the number of QDs  $m_{\text{unit}}$  is 5 and their radius  $R_s$  linearly increases from 1 to 1.8 with the same bias voltage  $V_s = 3$  applied. The lattice spacing  $d$  in (c)–(e) is 4. The incident electron beams have energy  $\tilde{E} = 0.48$ .

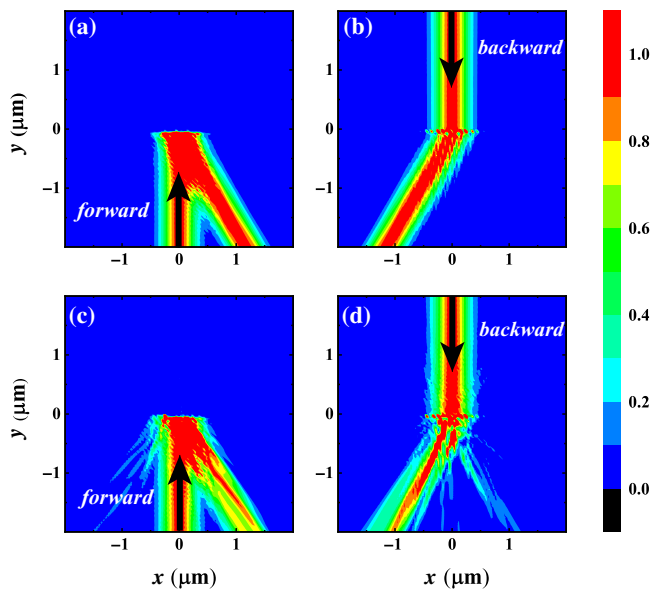


FIG. 5. Electron-density distribution around the composite when it is illuminated by a Gaussian beam in (a) [(c)] the forward-propagating direction and (b) [(d)] the backward-propagating direction without (with) the disorder of position. The composite is composed of the band-gap material and the metasurface shown in Fig. 4. The incident Gaussian beam has energy  $\tilde{E} = 0.48$ .

range. The normal-incidence backward-propagating electrons arrive directly at the band-gap material and penetrate through it because of Klein tunneling. The transmitted electrons subsequently strike the metasurface at normal incidence and finally travel out at a transmission angle of about  $30^\circ$ , as shown in Fig. 5(b). In brief, the composite has a broken spatial-inversion symmetry in its structure due to the presence of the metasurface, which imparts an added transverse momentum to change the propagation direction of the forward-propagating electrons. The backward-propagating electrons do not perceive transverse momentum before they encounter the band-gap material. Consequently, the band-gap material allows the normal-incidence backward-propagating electrons to pass through because of Klein tunneling while blocking the forward-propagating electrons because of the partial band gap. The composite is actually an array of QDs with as few as four layers. Such a few-layer design allows the relaxation of practical fabrication demands and the realization of compact components. The fabrication techniques for high-precision QD arrays [46] make it possible to experimentally demonstrate asymmetric transmission. Nanoscale circular QDs with an atomically sharp boundary [47,48] have been obtained in experiments by substrate engineering, which is a technique that does not damage the graphene lattice. As a result, the advantage of graphene's high mobility is preserved intact in asymmetric transmission.

In Figs. 5(c) and 5(d), we show the effect of QD-position disorder on asymmetric transmission with the other parameters unchanged. The displacement of each QD from its original position is expressed as  $d_i = \xi \chi d_{i0}$ , with  $i = x$  or  $y$ , where  $\xi$  is a random number uniformly distributed between  $-1$  and  $1$ ,  $d_{i0} = d/2 - R_s$  and  $d_{i0} = a/2 - R_s$  are, respectively, the maximum position variation in the metasurface and in the band-gap material, and  $\chi$  is a quantity measuring the degree of disorder, which should be set to be 1 or less than 1 to avoid the overlapping of neighboring QDs. In Figs. 5(c) and 5(d),  $\chi = 0.4$  is chosen. We see that asymmetric transmission of electrons is not nearly affected by the disorder. Usually the QD position can be well controlled in periodic structures in actual experiments, and its disorder is less than our assumption above. In addition, the band-gap material and the metasurface do not necessarily require circular quantum dots. In practical processing, it is more likely that the shapes of all quantum dots will undergo an overall shift. This generally does not lead to the disappearance of asymmetric transmission, but the operating energy may change accordingly.

In the above-mentioned simulations, the QD radius  $R_s$  is set to be 1, which implies that the quantities with the dimension of length, including the lattice spacing and wavelength, are in unit of  $R_s$ . When  $R_s$  in real units is given, the lattice spacings of the band-gap material and the metasurface are  $a = 5R_s$  and  $d = 4R_s$ , respectively. The wavelength  $\lambda$  is  $2\pi R_s/E$ , and thus the incident energy and the bias voltage in real units are  $E\hbar v_F/R_s$  and  $V_s\hbar v_F/R_s$ , respectively, according to the de Broglie relationship. Typically, the QDs used in the band-gap material and the metasurface have radius  $R_s = 5$  nm, and thus the incident energy is 79.4 meV. The lattice spacing and the bias voltage applied on the QDs are 25 nm and 394.9 meV, respectively, in the band-gap material. The QDs in each unit cell of the metasurface have radius linearly increasing from 5 to 9 nm. The spacing and the bias voltage are 20 nm and 394.9 meV, respectively. The total thickness of the four-layer structure is thus 75 nm, much smaller than the existing designs, which typically range from hundreds of nanometers to several micrometers [3,6,8,10,49].

In summary, we have theoretically demonstrated the possibility of achieving asymmetric transmission for low-energy ballistic electrons in graphene. A simple four-layer array of QDs is used to achieve this aim. One layer functions as an electron metasurface, with its unit cell composed of radius-varying QDs, and is responsible for introducing breaking of spatial-inversion symmetry by presenting a lateral momentum. The other three layers provide a partial band gap to block the transmission of oblique-incidence electrons. The backward-propagating electrons that directly impinge normally on the band-gap material pass through the band-gap material and further the metasurface by means of Klein tunneling, whereas the forward-propagating electrons are converted

into oblique incidence by the metasurface and are totally reflected. Nonreciprocal transmission provides possibilities to explore applications associated with one-way states within the framework of Dirac fermions, as well as on the graphene platform.

- 
- [1] A. K. Geim and K. S. Novoselov, *Nat. Mater.* **6**, 183 (2007).
- [2] P. Bøggild, *et al.*, *Nat. Commun.* **8**, 15789 (2017).
- [3] K. Wang, *et al.*, *Proc. Nat. Acad. Sci.* **116**, 6575 (2019).
- [4] A. V. Shytov, *et al.*, *Phys. Rev. Lett.* **101**, 156804 (2008).
- [5] J. R. Williams, *et al.*, *Nat. Nanotechnol.* **6**, 222 (2011).
- [6] M. Kim, *et al.*, *Nat. Phys.* **12**, 1022 (2016).
- [7] M.-H. Liu, *et al.*, *Phys. Rev. Lett.* **118**, 066801 (2017).
- [8] J. Li, *et al.*, *Science* **362**, 1149 (2018).
- [9] V. V. Cheianov, *et al.*, *Science* **315**, 1252 (2007).
- [10] S. W. Chen, *et al.*, *Science* **353**, 1522 (2016).
- [11] G.-H. Lee, *et al.*, *Nat. Phys.* **11**, 925 (2015).
- [12] B. Brun, *et al.*, *Phys. Rev. B* **100**, 041401(R) (2019).
- [13] Y.-W. Son, *et al.*, *Phys. Rev. Lett.* **97**, 216803 (2006).
- [14] J. O. Sofo, *et al.*, *Phys. Rev. B* **75**, 153401 (2007).
- [15] R. Martinazzo, S. Casolo, and G. F. Tantardini, *Phys. Rev. B* **81**, 245420 (2010).
- [16] I. I. Naumov and A. M. Bratkovsky, *Phys. Rev. B* **84**, 245444 (2011).
- [17] S. Y. Zhou, *et al.*, *Nat. Mater.* **6**, 770 (2007).
- [18] C. M. Zhang, *et al.*, *Phys. Rev. Lett.* **130**, 087001 (2023).
- [19] J. Zhao, *et al.*, *Nature* **625**, 60 (2024).
- [20] L. E. Foa Torres, *et al.*, *Phys. Rev. B* **93**, 075438 (2016).
- [21] V. Dal Lago, *et al.*, *Phys. Rev. B* **96**, 235409 (2017).
- [22] K. Shiraishi, *et al.*, *Appl. Opt.* **23**, 1103 (1984).
- [23] D. Gauthier, *et al.*, *Opt. Lett.* **11**, 623 (1986).
- [24] Y. Shoji, *et al.*, *Appl. Phys. Lett.* **92**, 071117 (2008).
- [25] L. Bi, *et al.*, *Nat. Photonics* **5**, 758 (2011).
- [26] Z. Yu and S. Fan, *Nat. Photonics* **3**, 91 (2009).
- [27] M. S. Kang, *et al.*, *Nat. Photonics* **5**, 549 (2011).
- [28] H. Lira, *et al.*, *Phys. Rev. Lett.* **109**, 033901 (2012).
- [29] K. Fang, *et al.*, *Phys. Rev. Lett.* **108**, 153901 (2012).
- [30] L. Tzuang, *et al.*, *Nat. Photonics* **8**, 701 (2014).
- [31] E. Li, *et al.*, *Nat. Commun.* **5**, 3225 (2014).
- [32] D. L. Sounas, *et al.*, *Nat. Commun.* **4**, 2407 (2013).
- [33] K. Xia, *et al.*, *Phys. Rev. Lett.* **121**, 203602 (2018).
- [34] L. Tang, *et al.*, *Photonics Res.* **9**, 1218 (2021).
- [35] X. Li, *et al.*, *Phys. Rev. Lett.* **106**, 084301 (2011).
- [36] Y. Li, *et al.*, *Phys. Rev. Lett.* **119**, 035501 (2017).
- [37] M. I. Katsnelson, *et al.*, *Nat. Phys.* **2**, 620 (2006).
- [38] R. Zhao, *et al.*, *Phys. Rev. B* **107**, 155404 (2023).
- [39] F. Ghahari, *et al.*, *Science* **356**, 845 (2017).
- [40] J. Lee, *et al.*, *Nat. Phys.* **12**, 1032 (2016).
- [41] Y. Ren, *et al.*, *Phys. Rev. B* **103**, 085431 (2021).
- [42] See Supplemental Material at <http://link.aps.org/supplemental/10.1103/PhysRevApplied.22.L031003>, in which Refs. [50–60] are cited, where we present the following: (1) the spherical wave basis of eigenstates of the single-valley Dirac-Hamiltonian, (2) the Mie-scattering method and the multiple-scattering method, and (3) the phase jump in the metasurface at  $\theta_i = 0$  and  $\theta_i = 30^\circ$ .
- [43] A. Pieper, *et al.*, *Europhys. Lett.* **104**, 47010 (2013).
- [44] A. W. Barnard, *et al.*, *Nat. Commun.* **8**, 15418 (2017).
- [45] N. Yu, *et al.*, *Science* **334**, 333 (2011).
- [46] J. M. Caridad, *et al.*, *Nat. Commun.* **7**, 12894 (2016).
- [47] K. Bai, *et al.*, *Phys. Rev. B* **97**, 045413 (2018).
- [48] C. Gutiérrez, *et al.*, *Nat. Phys.* **12**, 1069 (2016).
- [49] P. Rickhaus, *et al.*, *Nano Lett.* **15**, 5819 (2015).
- [50] R. L. Heinisch, *et al.*, *Phys. Rev. B* **87**, 155409 (2013).
- [51] C. Schulz, *et al.*, *Phys. Rev. B* **91**, 045130 (2015).
- [52] M. I. Katsnelson, *et al.*, *Phys. Rev. B* **79**, 195426 (2009).
- [53] M. Hentschel and F. Guinea, *Phys. Rev. B* **76**, 115407 (2007).
- [54] D. S. Novikov, *Phys. Rev. B* **76**, 245435 (2007).
- [55] J. Cserti, *et al.*, *Phys. Rev. Lett.* **99**, 246801 (2007).
- [56] P. M. Ostrovsky, *et al.*, *Phys. Rev. B* **74**, 235443 (2006).
- [57] Y. Ren, *et al.*, *Phys. Rev. B* **100**, 045422 (2019).
- [58] Y. Tang, *et al.*, *Sci. Rep.* **6**, 33522 (2016).
- [59] J. Korringa, *Physica* **13**, 392 (1947).
- [60] W. Kohn and N. Rostoker, *Phys. Rev.* **94**, 1111 (1954).